RSC Advances

ROYAL SOCIETY OF CHEMISTRY

www.rsc.org/advances

completely new materials[14-19] or the impartment of well-properties and innovative morphologies.[20-22] However, fewer efforts have been dedicated to exploring mixed-phase photocatalysts with the favored structure, despite their known photoreactivity.

On the other hand, the as-synthesized photocatalysts normally exist in the form of powders that are inconvenient to be separated from the reaction system. A solution to the problem is to load the powdered photocatalysts on the recyclable substrates.[23, 24] Recently, paper and paper-like substrates have fascinated researchers to fabricate paper-based energy and electronics devices, based on nanoparticles, thin films, and the transfer of one-dimensional and two-dimensional nanostructures. The prototype devices, such as paper batteries and supercapacitors,[25] thin film transistors,[26] electronic paper displays,[27] printed circuit boards,[28] and active-matrix organic light emitting diodes, exhibit exceptional technological attributes and commercial perspectives. Similarly, paper should be also the desired substrate for loading the photoreactive materials to form photocatalytic papers,[29, 30] because the procedures for manufacturing the photocatalytic papers can be straightforward (printing, spraying, etc.) and consequently should be relatively inexpensive and be easy to scale up. In addition, papers consisting of cellulose fibers have three-dimensional network structure, which provides high-density meshes to accommodate the photoreactive materials. Relative to the maturity and diversity of paper-based energy and electronics devices, only a limited number of photocatalytic papers have been shown to date, and most of them are fabricated by directly applying tiny colloidal nanoparticles (e.g., P25 TiO_2) onto the paper.[29] However, the sizes of the cellulose networks in the paper are usually dozens of times that of tiny nanoparticles. Such a tremendous size difference cannot guarantee the nanoparticles to attach to the paper securely. In this regard, tiny colloidal nanoparticles are not the suitable photocatalysts for manufacturing photocatalytic papers.

To design an efficient and recyclable photocatalyst with the above factors in mind, herein, we first report the deterministic synthesis of mixed-phase hollow spheres organized by Fe_2O_3 and ZnO nanoparticles. Both ZnO and Fe_2O_3 belong to earth-abundant photocatalysts with good activity.[31-35] Interestingly, the shells of the Fe_2O_3/ZnO hollow spheres have submicron hole, which is the first report for such a system. The innovative morphology endows the hollow spheres with the property of rapidly gathering pollutants from the contaminated water. Then, we demonstrate the application of the aqueous dispersion of Fe_2O_3/ZnO hollow spheres as the printable ink for known materials (e.g., TiO_2, Fe_2O_3, ZnO) with synergistic manufacturing photocatalytic papers. The Fe_2O_3/ZnO hollow spheres show a perfect geometric match to the cellulose networks within the paper due to the close dimensions. Finally, as a conceptual demonstration of the target application as the solar-driven photocatalyst, we use the photocatalytic paper to degrade 2,4,6-trichlorophenol (TCP), which represents the largest class of chlorinated persistent pollutant responsible for the contamination of potential drinking water sources around the world.[36]

Experimental

Chemicals

All reagents were purchased from Shanghai Chemical Co. and used as received.

Preparation of the Fe_2O_3/ZnO hollow spheres

In a typical synthesis, 0.135 g $FeCl_3 \cdot 6H_2O$ (0.5 mmol) and 0.11 g $Zn(Ac)_2 \cdot 2H_2O$ (0.5 mmol) were dissolved in 10 ml of absolute ethanol, and then 0.1g anhydrous NaAc was added under the magnetic stirring. The mixture was transferred to a 20 ml of Teflon-lined autoclave and heated at 190 °C for 24 hours. After cooled down to ambient temperature, brown solid was collected from the autoclave, thoroughly washed with 95% ethanol to remove the impurities, and dried at ambient temperature.

Adsorption study

For adsorption, the Fe_2O_3/ZnO hollow spheres (10 mg) were added to 5 mL aqueous solution contained fluorescein (1 mg/L) or TGA stabilized CdTe quantum dots (QDs) (TGA = thioglycolic acid). After shaken at ambient temperature for 15 min, the Fe_2O_3/ZnO hollow spheres were separated from the solution by centrifugation and washed three times with distilled water to remove free fluorescein or QDs. The hollow spheres were then deposited onto the surface of a glass slide and observed under an Olympus IX-71 fluorescence microscope.

Characterizations

Transmission electron microscopy (TEM) and high-resolution transmission electron microscopy (HRTEM) characterizations were performed on an FEI Tecnai G20 electron microscope operating at the accelerating voltage of 200 kV. Scanning electron microscopy (SEM) measurements were performed on a HITACHI S4800 electron microscope operating at the accelerating voltage of 20 kV. X-ray diffraction measurements were performed on a Panalytical X'Pert PRO diffractometer. Elemental analysis and mapping were performed on the energy dispersive X-ray spectrometers equipped on the

Journal Name

ARTICLE

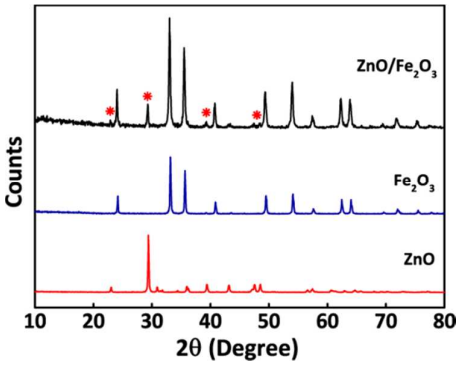

Fig. 1. XRD patterns for the synthesized ZnO/Fe_2O_3 hollow spheres and commercial ZnO and Fe_2O_3 nanoparticles.

scanning electron microscope. X-ray photoelectron spectroscopy (XPS) were performed on an ESCALAB MK II X–ray photoelectron spectrometer) using an Al Kα source. Shimadzu 3150 UV-vis-near-infrared spectrophotometer equipped with an integrating sphere was used to record the diffusion reflection spectra of the samples. Alternating current impedance measurements were carried out by a Zahner Im6ex instrument under the following conditions: ac voltage amplitude 5 mV, frequency ranges 0.01 Hz to 100 kHz, and open circuit.

Manufacture of the photocatalytic paper

First, the dried Fe_2O_3/ZnO hollow spheres were re-dispersed in distilled water to give a homogeneous dispersion (concentration: 0.5 g/L). The dispersion was then sprayed onto the commonly used filter paper by a household sprayer. The resulted photocatalytic paper was left to dry at 50°C. The spraying and drying process was done three to five times, and finally the brown photocatalytic paper with equal color distribution was obtained. By measuring the weight of the paper before and after the loading, the mass per unit area for the hollow spheres is calculated to be ca. 0.2 g/m^2.

The reactivity of the photocatalytic paper was assessed by the photodegradation of TCP. In each test, a piece of 10×10 cm^2 paper was immersed in 200 mL aqueous solution of TCP (0.1 g/L). The solution was first left to stand for 30 min in the dark to allow the adsorption equilibrium of TCP on the photocatalytic paper. Then, the solution was illuminated with the stimulated solar light emitted from a 200 W Xe lamp, with the temperature kept at 25 °C. Samples were taken every 20 min and the concentration of TCP was measured by a high performance liquid chromatography (HPLC). For comparison, the photocatalytic experiments were performed by using the blank paper, the paper loaded with the pure-phase Fe_2O_3 hollow spheres (details about the synthesis are shown in the ESI), and the paper loaded with the simple mixture of Fe_2O_3 hollow spheres and ZnO nanocrystals (in a molar ratio of 3:1). In all control experiments, the area of the paper was also 10×10 cm^2 and the mass per unit area for the photocatalyst was controlled at 0.2 g/m^2.

Results and discussion,

Structure of the Fe_2O_3/ZnO hollow spheres

To prepare the mixed-phase Fe_2O_3/ZnO hollow spheres, we designed a co-precipitation solvothermal route, by using $FeCl_3$ and $Zn(Ac)_2$ as the sources, NaAc as the mineralizing agent, and absolute ethanol as the solvent. After the completion of the reaction in the autoclave, large amounts of brown solids with a high yield (ca. 95%) were harvested. The product was firstly checked by XRD to clarify the phase composition (Fig. 1). We also acquired the XRD data of commercial ZnO and Fe_2O_3 nanoparticles for phase reference (Fig. 1). The comparisons among the three XRD patterns clearly reveal the presence of hematite (α-Fe_2O_3) as the primary crystal phase of the product, with additional peaks corresponding to ZnO. Moreover, XPS analysis of the product confirmed the presence of α-Fe_2O_3 (ESI, Fig. S1). The result demonstrates that the product is the desired Fe_2O_3/ZnO in a mixed phase, rather than individual Fe_2O_3 or ZnO. Elemental analysis indicates that the molar ratio of Fe to Zn in the sample is around 3:1, which is three times higher than the initial feed ratio between $FeCl_3 \bullet 6H_2O$ and $Zn(Ac)_2 \bullet 2H_2O$. The reduction of Zn component in the system is associated with the growth mechanism of the Fe_2O_3/ZnO material, as will be explained below.

Fig. 2a-c displays the SEM data of the Fe_2O_3/ZnO sample, which reveal that the product is composed of spheres at the micron scale. Although no soft and hard templates were used

Journal Name

ARTICLE

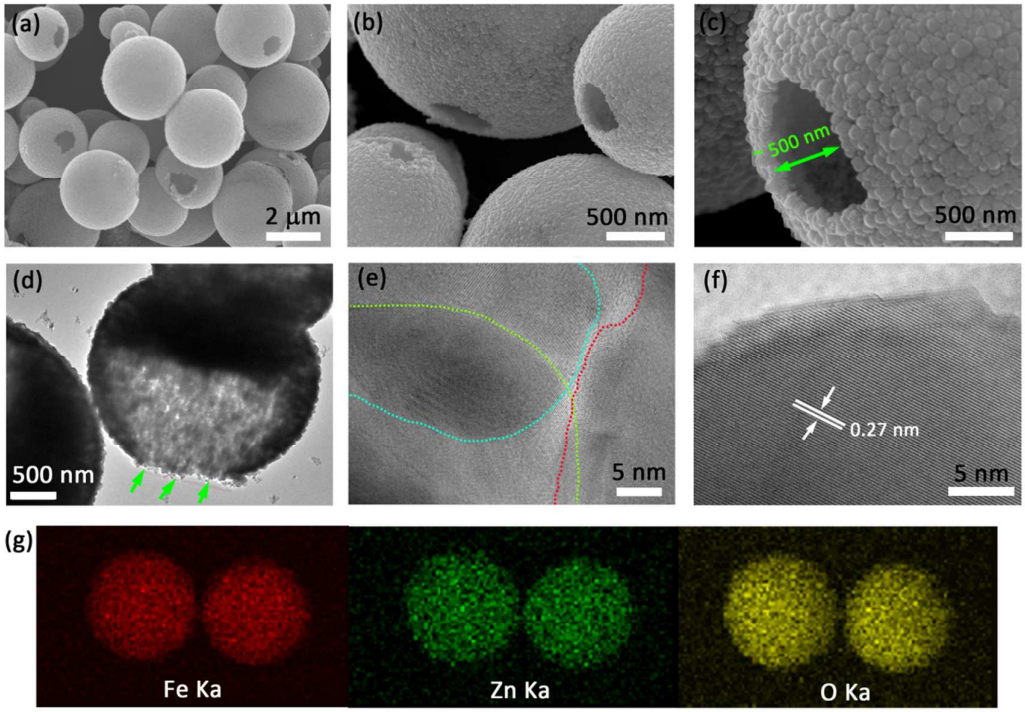

Fig. 2. (a-c) SEM images of the mixed-phase Fe_2O_3/ZnO hollow spheres. (d) TEM image of the Fe_2O_3/ZnO hollow spheres, where the arrows indicate the surface hole. (e, f) HRTEM images of the Fe_2O_3/ZnO hollow spheres, where the dot lines indicate the grain boundaries. (g) Elemental mapping of the Fe_2O_3/ZnO hollow spheres.

to confine the growth, the microspheres account for a high proportion in the product (> 90%) (ESI, Fig. S2). The high yield of the microspheres is attributed to the moderate alkaline environment created by NaAc, which is advantageous to the smooth mineralization of Fe^{3+} and Zn^{2+} ions and eventually leads to a uniform morphology. By measuring 200 arbitrarily chosen spheres in scanning electron micrographs, we acquired the sizes the microspheres, which are in the range of 0.5~5 μm (ESI, Fig. S3). Also, the SEM images reveal that the microspheres are formed via the self-organization of large amounts of polyhedral nanocrystallites (Fig. 2b and 2c). Interestingly, a submicron pore (~ 500 nm) is located on the shell of each microsphere. Through the pore, one can see that the microspheres are hollow and their shells are formed by a monolayer of nanocrystallites. This innovative morphology is highly wished in photocatalytic applications since the diffusion rates through the holes exceeding 10 nm are similar to the molecules in open media.[37] The low diffusion barrier will facilitate the contaminants to rapidly access both the external and internal surfaces of the hollow spheres, thus expanding the interface with the contaminated water for maximizing the reaction sites.

Fig. 2d shows a representative TEM image of the Fe_2O_3/ZnO hollow spheres; the truncated shell (indicated by the arrow) demonstrates the presence of surface hole and the contrast between the black shell and the pale central part is indicative of the hollow structure of the microsphere. Fig. 2e and 2f show the HRTEM characterizations of the Fe_2O_3/ZnO hollow spheres. The HRTEM image taken from multiple nanocrystallites reveals that the crystallites are fused in the microsphere (the dot lines indicate the grain boundaries) (Fig. 2e). In addition, the lattice fringes demonstrate that the nanoparticles are well crystallized, consistent with the XRD data. The HRTEM image taken from an individual nanoparticle further confirms the good crystallinity of the particles (Fig. 2f). Owing to the near interplanar spacing, it is difficult to identify the attribution of the individual nanoparticle to Fe_2O_3 or ZnO just from the lattice fringes. Consequently, the mapping of O, Fe, and Zn elements were recorded by the energy dispersive X-ray

Journal Name

ARTICLE

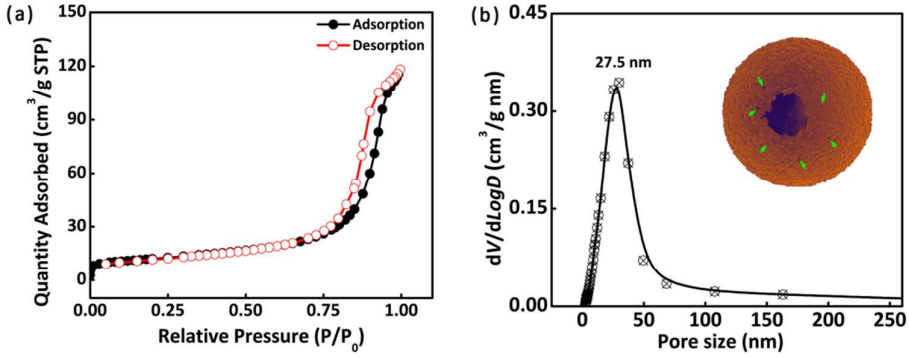

Fig. 3. (a) Nitrogen adsorption–desorption isotherms of the Fe_2O_3/ZnO hollow spheres at 77 K. (b) BJH pore-size distribution plots determined from the desorption branch. The mesopores are mainly arisen from the interparticle gaps, as indicated by the arrows in the inset.

analysis (Fig. 2g). The results show a homogeneous distribution of O, Fe, and Zn elements within the microsphere, demonstrating the intimate contact between the nanoparticles of Fe_2O_3 and ZnO.

It is worth mentioning that the component of ZnO in the Fe_2O_3/ZnO hollow spheres can be etched with ammonia through the following reaction (Eq. 1).

$$ZnO + 4NH_3 + H_2O \rightarrow [Zn(NH_3)_4)](OH)_2 \quad \text{(Eq. 1)}$$

Fig. S4 shows the XRD pattern of the microsphere after the etching treatment. The disappearance of the diffraction peaks at 2θ = 22.8°, 29.3°, 39.2°, and 47.3° suggests the complete removal of ZnO. Fortunately, the dissolution of ZnO did not bring adverse effects on the structures of the hollow spheres. As shown in Fig. S5, both the spherical morphology and the surface pores are well maintained. The above results demonstrate that the mixed-phased Fe_2O_3/ZnO hollow spheres can be readily converted into the pure-phase Fe_2O_3 hollow spheres. Owing to the basically identical structure, the pure-phase Fe_2O_3 hollow spheres may serve as the reference for studying the mixed-phase effects from the Fe_2O_3/ZnO hollow spheres.

Growth mechanism of the Fe_2O_3/ZnO hollow sphere

The formation of the open Fe_2O_3/ZnO hollow sphere with the innovative morphology can be explained by the combined effect of Ostwald ripening and amphoteric phenomenon (Fig. S6, ESI). Also, the solvothermal environment is indispensable. When $FeCl_3$ and $Zn(Ac)_2$ were mixed with weakly alkaline NaAc, Fe^{3+} and Zn^{2+} ions were readily precipitated to form Fe_2O_3 and ZnO crystallites (step i, Fig. S6). Owing to the exposure of abundant surfaces, the as-formed Fe_2O_3 and ZnO crystallites were thermodynamically unstable. Thus, they were inclined to spontaneously aggregate into mixed-phase microspheres to eliminate the surfaces and lower the free energy of the system (step ii, Fig. S6). At the initial stage, the microspheres comprised of the fine crystallites were intact and had a dense shell, as learned from the corresponding SEM image (Fig. S7a, ESI). It can be imaged that large amounts of ethanol molecules were enclosed in the microspheres. With the increase of the temperature of the reaction system, ethanol enclosed in the microspheres was expanded and eventually burst the microsphere to balance the pressure (step iii, Fig. S6). As a result, hole was formed on the shell of the microsphere. From the SEM image (Fig. S7b and S7c, ESI), it can be seen that the inside of the microsphere was still filled by nanocrystallites at this time. Subsequently, Ostwald ripening and amphoteric phenomenon would work (step iv, Fig. S6). On the one hand, owing to their higher surface energy, small crystallites within the microspheres were dissolved and merged into the larger particles in the outer surface.[38, 39] On the other hand, with the increase of the reaction temperature, parts of ZnO nanocrystallites were re-dissolved due to their amphoteric nature. This would further empty the intermediates, and at the same time, cause a relative low percentage of ZnO in the final product. Under the combination actions of Ostwald ripening and amphoteric phenomenon, the solid microsphere intermediates were gradually transformed into a hollow structure with the innovative surface hole.

Adsorption property of the Fe_2O_3/ZnO hollow sphere

Fig. 3 shows the characterizations of the mixed-phase Fe_2O_3/ZnO hollow spheres with the technique of nitrogen isothermal adsorption/desorption at 77 K. The isotherms display a hysteresis at a relatively high pressure (P/P_0 range: 0.7–1.0) but no plateau appears. These characteristics indicate the co-existence of mesopores and macropores

Journal Name

ARTICLE

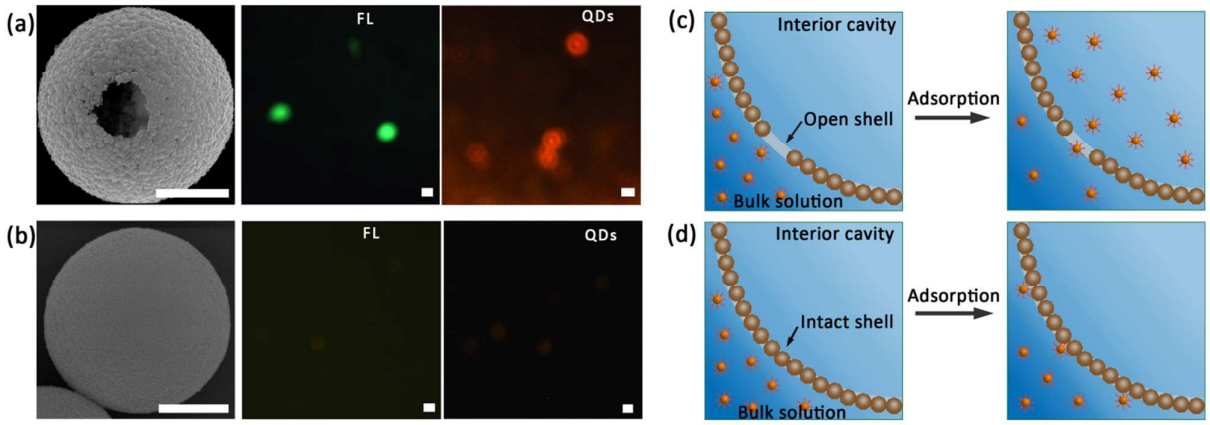

Fig. 4. Adsorption property studies by using fluorescein and QDs as the visual probes. (a) Fe_2O_3/ZnO hollow spheres with submicron pore. (b) Fe_2O_3/ZnO hollow spheres with intact shell. (c, d) Proposed adsorption mechanisms.

within the Fe_2O_3/ZnO hollow spheres, consistent with the SEM and TEM data. The BET surface area and total pore volume for the mixed-phase hollow spheres are 42.4 m^2/g and 0.18 cm^3/g, respectively. The relatively smaller BET surface area to the previously reported Fe_2O_3 hollow spheres is because the Fe_2O_3 and ZnO nanoparticles herein have a relatively large size.[40-42] Fig. 3b shows the pore size distributions calculated from the desorption branch of the isotherms using the Barrett-Joyner-Halenda (BJH) theory, which suggests that mesopores are overwhelming. The mesopores mainly arise from the gaps among the crystallites, as indicated by the inset in Figure 3b. This type of pores normally has a huge permeation resistance due to the tortuous microstructure and the wide pore size distribution,[43] which in general compromises their permeability and adsorption performance.

To gain deep insights into the porous feature and the associated adsorption behaviors of the Fe_2O_3/ZnO hollow spheres, we employed fluorescein molecules and CdTe QDs as the visual probes. The molecular size of fluorescein is about 11 Å,[44] which are close to the dimensions of some small pollutants (e.g., dyes and POPs). The particle size of QDs is about 35 Å, which are close to the dimensions of macromolecular and biological pollutants. Therefore, fluorescein and QDs are the suitable model pollutants to evaluate the adsorption performance of the Fe_2O_3/ZnO hollow spheres. For comparison, we also studied the adsorption behaviors of Fe_2O_3/ZnO microspheres with dense shell (as shown in Fig. S7a). After the impregnation in aqueous solution of fluorescein and QDs for a short period (15 min), the open Fe_2O_3/ZnO hollow spheres exhibit the bright fluorescence under the fluorescent microscope (Fig. 4a). In contrast, when the dense microspheres were examined under identical conditions, we only observed very weak fluorescence (Fig. 4b). The great disparity in the fluorescence intensity clearly suggests that the submicron pores on the shells of the Fe_2O_3/ZnO hollow spheres lead to a low permeation barrier, and hence, the hollow spheres are able to capture more fluorescein and QDs than the closed ones. The enhanced adsorption performance should be particularly helpful for the photocatalytic application of the Fe_2O_3/ZnO hollow spheres, because it can increase the pollutant concentration around the photoreactive sites.

Manufacture of the photocatalytic paper based on the mixed-phase Fe_2O_3/ZnO hollow sphere

Profiting from the hollow interiors, the mixed-phase Fe_2O_3/ZnO spheres are light-weight materials and are able to suspend in the water stably without the assistance of any organic dispersants (Fig. 5a). This inspires us that the aqueous dispersion of the hollow spheres can be used as the ink for the printable manufacture of photocatalytic paper. In the current study, we quickly prepared the photocatalytic paper by spraying the ink onto the common cellulose paper (Fig. 5a). Alternatively, one can use other established techniques such as inkjet printing and roll coating to deposit the hollow spheres with the well-defined geometries. As shown in Fig. 5a, the cellulose paper changes its color from the initial white to brown after the incorporation of the Fe_2O_3/ZnO hollow spheres (mass per unit area: ~ 0.2 g/m^2). The loading of the hollow spheres can be readily adjusted by controlling the spraying number or the concentration of the ink. Fig. 5b

Journal Name

ARTICLE

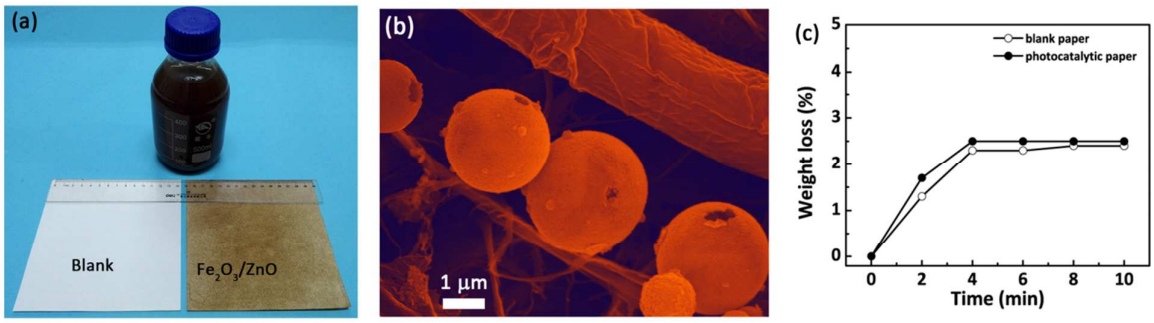

Fig. 5. Manufacture of the photocatalytic paper. (a) Photographs of the Fe2O3/ZnO hollow sphere dispersion and the photocatalytic paper fabricated by the spraying method. (b) SEM image of the photocatalytic paper. (c) Stability test of the photocatalytic paper by the nitrogen blowing method.

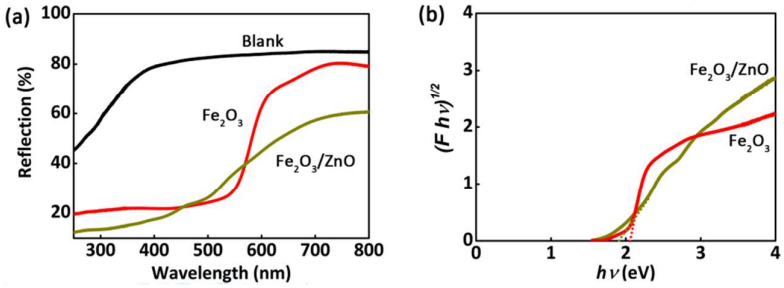

Fig. 6. (a) Diffuse reflection spectra of the blank paper and the photocatalytic papers based on the mixed–phase Fe_2O_3/ZnO hollow spheres and the pure–phase Fe_2O_3 hollow spheres. (b) Corresponding Tauc plots, with linear extrapolations to $(Fhv)^{1/2} = 0$.

shows the SEM image of the photocatalytic paper. The hollow spheres exactly stuck in the network and surround by the cellulose fibers due to the matching dimensions. This will prevent the hollow spheres from falling apart and guarantee the reliable performance of the photocatalytic paper. To further verify the tough combination of the hollow spheres with the substrate, nitrogen blowing experiments were carried out at a pressure of 2 bar for 10 min (Fig. 5c). As seen, the weight of the photocatalytic paper stops alternation after the slight weight loss at the first 4 min. The initial weight loss for the samples is attributed to the removal of the broken fibers resulting from the cutting process.

Fig. 6a displays the diffusion reflection spectra of the blank cellulose paper (dark curve) and the as-prepared photocatalytic paper (dark yellow curve). For the blank paper, it shows the negligible absorption in the region of visible light. In contrast, with the incorporation of the Fe_2O_3/ZnO hollow spheres, the paper is endowed with the ability to intensely absorb the lights below 650 nm, indicating that it is potential for target application as the visible light photocatalyst. To determine the band gap of the photocatalytic paper, $(Fhv)^{1/2}$ vs. photon energy (hv) are generated from the diffusion reflection spectrum (Fig. 6b). Therein, F is the Kubelka-Munk function of the diffuse reflectance; exponent *1/2* was employed because of the indirect optical transitions of α-Fe_2O_3.[45] By extrapolating the linear region in the plots of $(Fhv)^{1/2}$ vs. hv, the bandgap value of the photocatalytic paper is measured to be 1.95 eV, which corresponds to the bandgap energy for α-Fe_2O_3 (1.9 ~ 2.2 eV).[45]

In the control experiments, we fabricated the control photocatalytic paper with the same weight of pure-phase Fe_2O_3 hollow spheres (Fig. S5, ESI). Like the photocatalytic paper based on the mixed-phase Fe_2O_3/ZnO hollow spheres, the control photocatalytic paper also exhibits a wide light harvesting range (red curve, Fig. 6a). By using the Kubelka-Munk method, the bandgap of the control photocatalytic paper is found to be 2.07 eV (Fig. 6b), which is also typical for α-Fe_2O_3.

Journal Name

ARTICLE

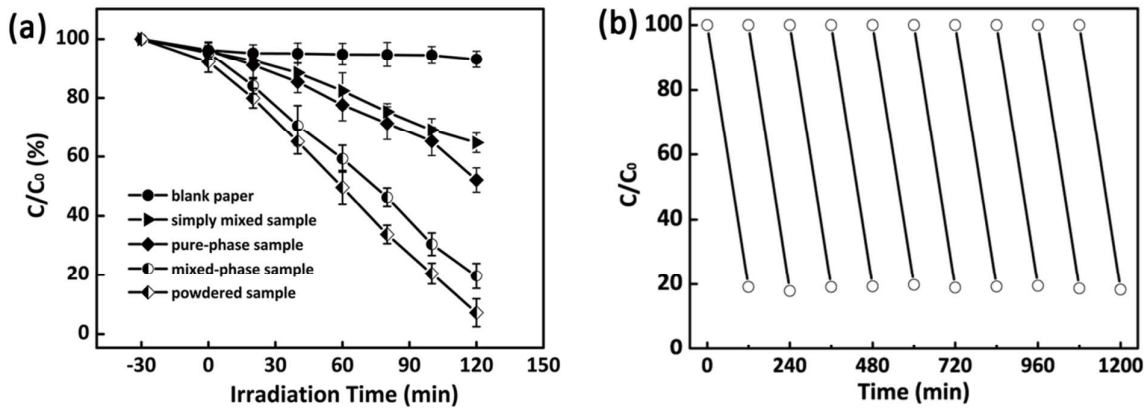

Fig. 7. (a) Photodegradation curves of TCP over the powdered Fe_2O_3/ZnO hollow spheres, blank paper, and the photocatalytic papers fabricated with the mixed–phase Fe_2O_3/ZnO hollow spheres, pure–phase Fe_2O_3 hollow spheres, and the simple mixture of Fe_2O_3 hollow spheres and ZnO nanoparticles. The bar plots are averages of five replicates and error bars are the standard deviations (b) Ten cycles of TCP photodegradation over the photocatalytic paper based on the mixed–phase Fe_2O_3/ZnO hollow spheres.

Photoreactivity of the photocatalytic paper

TCP is classified as *Group B2* (probable human carcinogen) by the United States Environmental Protection Agency,[46] which has been found in global fresh water. It is now urgent to find an efficient and cost-saved way to degrade TCP from the point of providing access to safe drinking water. Consequently, we chose the photocatalytic degradation of TCP to evaluate the performance of the as-prepared photocatalytic paper and the control samples (Fig. 7a). We firstly checked the photocatalytic performance of the powdered Fe_2O_3/ZnO hollow spheres (without the support of the cellulose paper). TCP was found to be degraded 95% over the course of a 120 min reaction time, demonstrating the high efficiency of the mixed-phase hollow spheres. By comparing the decay rate of TCP, it can be learned that the performance of the Fe_2O_3/ZnO hollow spheres is comparable to that of colloidal TiO_2.[47-49] Colloidal TiO_2, however, required the irradiation of intense UV light. The photocatalytic paper based on the Fe_2O_3/ZnO hollow spheres also exhibited high photocatalytic efficiency. At the same period of time, TCP decay was about 81%, corresponding to a first order rate constant of 0.014 min^{-1}. The slight decrease of the photocatalytic efficiency of the photocatalytic paper is understandable, because the unsupported Fe_2O_3/ZnO hollow spheres can be homogeneously dispersed in the solution and consequently offers more active sites. Besides the good photoreactivity, another important criterion for a good photocatalyst is high durability. To assess this, we cycled our photocatalytic paper consecutively for ten cycles (each cycle lasts 120 min). After each cycle, the photocatalytic paper was washed and dried thoroughly, and then fresh TCP solution was supplemented. As shown in Fig. 7b, the photodegradation rate of TCP remained constant, indicating that the performance of the photocatalytic paper is reliable under the irradiation of the simulated solar light. After the ten cycles of test, the photocatalytic paper was characterized by SEM and XRD. Both the data are identical to those acquired before the test (Fig. S8, ESI), suggesting the inherent stability of the mixed-phase Fe_2O_3/ZnO hollow spheres.

In the control experiments, the concentration of TCP was only decreased by 5.1% after a 120 min reaction time in the presence of the blank paper (Fig. 7a), which is known to be attributed to the adsorption of the paper. Thus, blank cellulose paper itself is not photoreactive and cannot remove TCP in the water under the current experiment condition. When the paper loaded with pure phase Fe_2O_3 hollow spheres was employed, the decay of TCP was increased to 48% over the course of 120 min reaction time (Fig. 7a). The result suggests the photoreactivity of nanostructured Fe_2O_3, consistent with previous findings.[31, 32, 40-42] However, when compared to the mixed-phase Fe_2O_3/ZnO hollow spheres, the decay rate of TCP on pure-phase Fe_2O_3 hollow spheres is roughly half (rate constant: 0.005 min^{-1} vs. 0.014 min^{-1}). The contrast indicates that the interactions of Fe_2O_3 with ZnO enhance the photocatalytic reactivity of the hollow spheres [33]. In another control experiment, we simply mixed the pure-

Journal Name

ARTICLE

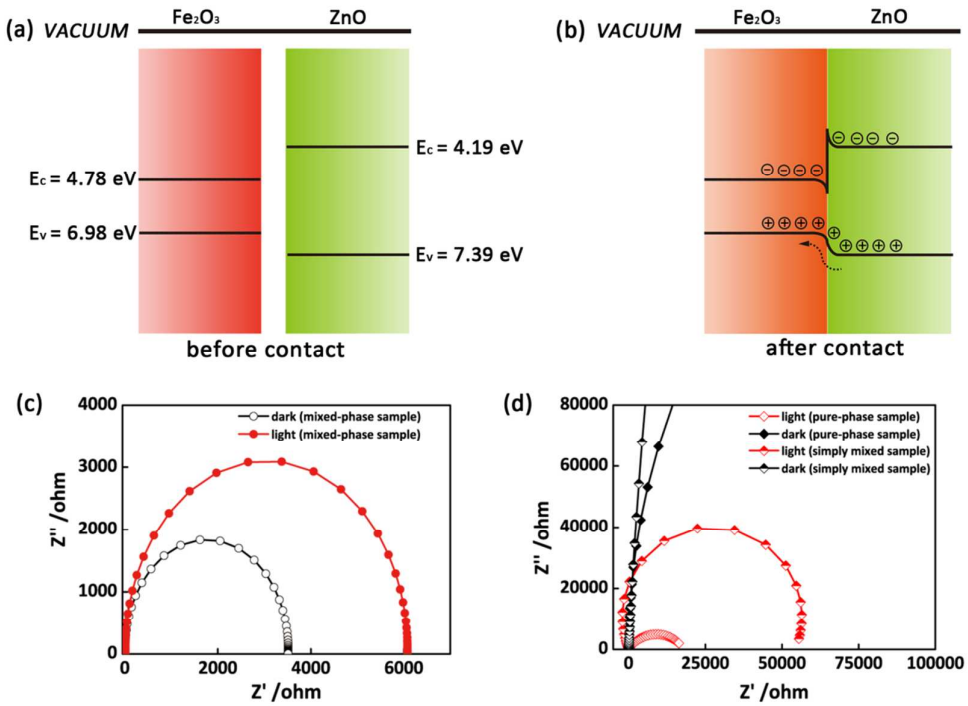

Fig. 8. Schematic for (a) energy bands of ZnO and Fe_2O_3 before contact and (b) the formation of type-I junction in a straddling configuration after contact. (c) Nyquist plots for the mixed-phase Fe_2O_3/ZnO hollow spheres. (d) Nyquist plots for the pure-phase Fe_2O_3 hollow spheres and the simple mixture of Fe_2O_3 hollow spheres and ZnO nanoparticles.

phase Fe_2O_3 hollow spheres with commercial ZnO nanoparticles in atomic ratio of 3:1, and sprayed the mixture onto the cellulose paper (Note: the same solvothermal treatment was applied to ZnO nanoparticles prior to the spraying). The photoreactivity of the mixture-based photocatalytic paper is similar to that based on pure Fe_2O_3, and is substantially lower than that based on Fe_2O_3/ZnO hollow spheres (rate constant: 0.004 min^{-1} vs. 0.014 min^{-1}). The results clearly demonstrate that, when ZnO and Fe_2O_3 nanoparticles are simply mixed in the system without the close interphase contact, TCP decay is not enhanced. Consequently, the close coupling of Fe_2O_3 and ZnO in the hollow spheres should play a critical role in enhancing the photoreactivity.[12]

The close coupling of Fe_2O_3 and ZnO in the mixed-phase hollow spheres can be theoretically explained. As shown in Fig. 8a and 8b, the intimate contact of the n-type ZnO with Fe_2O_3 will lead to the formation of a type-I heterojunction in a straddling configuration. The relative position of the Fe_2O_3 valence band edge permits the transfer of holes from ZnO, while the potential well on the Fe_2O_3 side and the potential barrier on the ZnO side hinder the transfer of photo-excited electrons. As a result, holes and electrons will be accumulated in Fe_2O_3 and around the solid-solid interfaces, respectively, which separate the charges and prevent them from recombination. The separated electrons will react with electron acceptors (e.g., O_2) and holes with electron donors (e.g., H_2O) to yield active free radicals (•OH, O_2^-•, etc.). Subsequently, TCP molecules are attacked by the generated free radicals, leading to the dechlorination and ring open reactions. As a result, the byproducts such as phenol, maleic acid, and oxalic acid were measured.

Besides the speculations, EIS measurements provide experimental evidences for supporting the enhanced charge transfer in the mixed-phase Fe_2O_3/ZnO hollow spheres.[50] Fig. 8c depicts the Nyquist plots for the mixed-phase Fe_2O_3/ZnO hollow spheres, which were recorded at the open circuit potential (OCP) over the frequency range of 100,000 to 0.1 Hz with sinusoidal perturbation of ± 5 mV. According to the distinct semicircle, the charge transfer resistance for the Fe_2O_3/ZnO hollow spheres in the dark is estimated to be 6100

Ω. When the Fe_2O_3/ZnO hollow spheres were illuminated by the simulated solar light, the size of the impedance arc is reduced to 3500 Ω. This phenomenon is attributed to the injection of abundant photogenerated electrons from the hollow spheres to the back contact and the migration of the holes to the hollow spheres/electrolyte interface. In response, the charge transfer resistance and the size of the arc radius on the Nyquist plots are reduced. Under the identical illumination conditions, pure-phase Fe_2O_3 hollow spheres show a charge transfer resistance of 18000 Ω, around 5 times larger than that for the mixed-phase sample (Fig. 8d). The difference indicates the indispensability of the heterojunctions in efficiently separating the photogenerated charges. As for the simple mixture of Fe_2O_3 and ZnO, it affords the largest charge transfer resistance (59000 Ω under the illumination condition). The result is understandable because Fe_2O_3 is not in intimate contact with ZnO in the simply mixed sample and additional barriers arise from the inter-particle charge transport, which has to occur by hopping and tunneling.[51] The above EIS data highlight the efficient charge separation in the mixed-phase Fe_2O_3/ZnO hollow spheres before the recombination takes place. In return, the photoreactivity of the Fe_2O_3/ZnO hollow spheres is enhanced relative to the pure-phase Fe_2O_3 hollow spheres and the simple mixture of Fe_2O_3 and ZnO.

Conclusions

We have demonstrated the successful synthesis of the mixed-phase Fe_2O_3/ZnO hollow spheres that are particularly suitable for the large-scale manufacture of photocatalytic paper. First, the hollow spheres have submicron holes on the shells; this morphological feature makes their interior and exterior surfaces both be readily accessible and enables them to enrich small and large pollutants rapidly. Second, the intimate contact between narrow bandgap Fe_2O_3 and wide bandgap ZnO leads to the emergence of the mixed-phase effect (e.g., enhanced charge separation and transfer) and the expansion of the light-collection range (spanning the full ultraviolet-visible wavelength), both of which are highly desired for the target application as visible light photocatalyst. Finally, since the hollow spheres are geometrically matched to the cellulose networks within the paper, they are easily incorporated into the paper substrate with a tough combination by the spraying method. The tests of the performances of the photocatalytic paper demonstrate that it can efficiently degrade TCP under the irradiation of the solar light. After ten recycles of the TCP photodegradation, the photocatalytic paper retains the constant activity, proving its high stability and durability. As a whole, the photocatalytic paper can be more readily recycled than conventional powder photocatalysts, and should be promising for various environmental applications, including water and air purification. More broadly, it may also be useful for the carbon-based photoanode of dye-sensitized solar cells after the graphitization of the photocatalytic paper.

Acknowledgements

This work is supported by the NSFC under Grant No. 21473079 and Science Technology Department of Zhejiang Province under Grant No. 2015C37010.

Notes and references

1. G. S. Omenn, *Science*, 2006, **314**, 1696-1704.
2. M. A. Shannon, P. W. Bohn, M. Elimelech, J. G. Georgiadis, B. J. Marinas and A. M. Mayes, *Nature*, 2008, **452**, 301-310.
3. W. Zhang, F. Jiang and J. Ou, *Proc. Inter. Acad. Ecol. Environ. Sci.*, 2011, **1**, 125-144.
4. D. Lapworth, N. Baran, M. Stuart and R. Ward, *Environ. Pollut.*, 2012, **163**, 287-303.
5. K. E. O'Shea and D. D. Dionysiou, *J. Phys. Chem. Lett.*, 2012, **3**, 2112-2113.
6. J. L. Wang and L. J. Xu, *Crit. Rev. Env. Sci. Technol.*, 2012, **42**, 251-325.
7. S. H. S. Chan, T. Yeong Wu, J. C. Juan and C. Y. Teh, *J. Chem. Technol. Biotechnol.*, 2011, **86**, 1130-1158.
8. M. Agulló-Barceló, M. Polo-López, F. Lucena, J. Jofre and P. Fernández-Ibáñez, *Appl. Catal. B* 2013, **136**, 341-350.
9. U. I. Gaya and A. H. Abdullah, *J. Photochem. Photobiol. C* 2008, **9**, 1-12.
10. C. Chen, W. Ma and J. Zhao, *Chem. Soc. Rev.*, 2010, **39**, 4206-4219.
11. H. Wang, L. Zhang, Z. Chen, J. Hu, S. Li, Z. Wang, J. Liu and X. Wang, *Chem. Soc. Rev.*, 2014, **43**, 5234-5244.
12. Y. Yao, G. Li, S. Ciston, R. M. Lueptow and K. A. Gray, *Environ. Sci. Technol.*, 2008, **42**, 4952-4957.
13. D. Hurum, A. Agrios, S. Crist, K. Gray, T. Rajh and M. Thurnauer, *J. Electron. Spectrosc. Relat. Phenom.*, 2006, **150**, 155-163.
14. S. Yan, Z. Li and Z. Zou, *Langmuir*, 2009, **25**, 10397-10401.
15. X. Wang, K. Maeda, X. Chen, K. Takanabe, K. Domen, Y. Hou, X. Fu and M. Antonietti, *J. Am. Chem. Soc.*, 2009, **131**, 1680-1681.
16. Y. Bi, S. Ouyang, N. Umezawa, J. Cao and J. Ye, *J. Am. Chem. Soc.*, 2011, **133**, 6490-6492.
17. K.-L. Zhang, C.-M. Liu, F.-Q. Huang, C. Zheng and W.-D. Wang, *Appl. Catal. B* 2006, **68**, 125-129.
18. J. Jiang, K. Zhao, X. Xiao and L. Zhang, *J. Am. Chem. Soc.*, 2012, **134**, 4473-4476.
19. M. Guan, C. Xiao, J. Zhang, S. Fan, R. An, Q. Cheng, J. Xie, M. Zhou, B. Ye and Y. Xie, *J. Am. Chem. Soc.*, 2013, **135**, 10411-10417.
20. D. Fattakhova-Rohlfing, A. Zaleska and T. Bein, *Chem. Rev.*, 2014, **114**, 9487-9558.
21. X. Cao, Z. Lu, L. Zhu, L. Yang, L. Gu, L. Cai and J. Chen, *Nanoscale*, 2014, **6**, 1434-1444.
22. L. Zhu, L. Gu, Y. Zhou, S. Cao and X. Cao, *J. Mater. Chem.*, 2011, **21**, 12503-12510.
23. P. Chen, L. Gu, X. Xue, M. Li and X. Cao, *Chem. Commun.*, 2010, **46**, 5906-5908.

24. L. Yang, Z. Hong, J. Wu and L.-W. Zhu, *RSC Advances*, 2014, **4**, 25556-25561.
25. B. Scrosati, *Nat. Nanotechnol.*, 2007, **2**, 598-599.
26. A. Manekkathodi, M. Y. Lu, C. W. Wang and L. J. Chen, *Adv. Mater.*, 2010, **22**, 4059-4063.
27. M. Nogi and H. Yano, *Adv. Mater.*, 2008, **20**, 1849-1852.
28. D.-H. Kim, Y.-S. Kim, J. Wu, Z. Liu, J. Song, H.-S. Kim, Y. Y. Huang, K.-C. Hwang and J. A. Rogers, *Adv. Mater*, 2009, **21**, 3703-3707.
29. R. Pelton, X. Geng and M. Brook, *Adv. Colloid Interface Sci.* , 2006, **127**, 43-53.
30. S. Baruah, M. Jaisai, R. Imani, M. M. Nazhad and J. Dutta, *Sci. Technol. Adv. Mater.*, 2010, **11**, 055002.
31. G. Liu, Q. Deng, H. Wang, D. H. Ng, M. Kong, W. Cai and G. Wang, *J. Mater. Chem.*, 2012, **22**, 9704-9713.
32. P. Xu, G. M. Zeng, D. L. Huang, C. L. Feng, S. Hu, M. H. Zhao, C. Lai, Z. Wei, C. Huang and G. X. Xie, *Sci. Total Environ.* , 2012, **424**, 1-10.
33. W. Wu, S. Zhang, X. Xiao, J. Zhou, F. Ren, L. Sun and C. Jiang, *ACS Appl. Mater. Inter.* , 2012, **4**, 3602-3609.
34. X. Cao, L. Gu, X. Lan, C. Zhao, D. Yao and W. Sheng, *Mater. Chem. Phys.*, 2007, **106**, 175-180.
35. J. Ran, J. Zhang, J. Yu, M. Jaroniec and S. Z. Qiao, *Chem. Soc. Rev.*, 2014, **43**, 7787-7812.
36. S. R. Lewis, S. Datta, M. Gui, E. L. Coker, F. E. Huggins, S. Daunert, L. Bachas and D. Bhattacharyya, *Proc. Natl. Acad. Sci. USA*, 2011, **108**, 8577-8582.
37. D. R. Rolison, *Science*, 2003, **299**, 1698-1701.
38. X. B. Cao, L. Gu, L. J. Zhuge, W. J. Gao, W. C. Wang and S. F. Wu, *Adv. Funct. Mater.*, 2006, **16**, 896-902.
39. H. G. Yang and H. C. Zeng, *J. Phys. Chem. B*, 2004, **108**, 3492-3495.
40. S.-W. Cao, Y.-J. Zhu, M.-Y. Ma, L. Li and L. Zhang, *J. Phys. Chem. C*, 2008, **112**, 1851-1856.
41. L. Li, Y. Chu, Y. Liu and L. Dong, *J. Phys. Chem. C*, 2007, **111**, 2123-2127.
42. Z. Wei, R. Xing, X. Zhang, S. Liu, H. Yu and P. Li, *ACS Appl. Mater. Inter.*, 2012, **5**, 598-604.
43. M. E. Warkiani, A. A. S. Bhagat, B. L. Khoo, J. Han, C. T. Lim, H. Q. Gong and A. G. Fane, *ACS nano*, 2013, **7**, 1882-1904.
44. J. Zhu, L. Zhu, Z. Lu, L. Gu, S. Cao and X. Cao, *J. Phys. Chem. C*, 2012, **116**, 23075-23082.
45. D. A. Wheeler, G. Wang, Y. Ling, Y. Li and J. Z. Zhang, *Energy Environ. Sci.*, 2012, **5**, 6682-6702.
46. *"2,4,6 Trichlorophenol". United States Environmental Protection Agency. Jan 2004*.
47. D. D. Dionysiou, A. P. Khodadoust, A. M. Kern, M. T. Suidan, I. Baudin and J.-M. Laîné, *Appl. Catal. B* 2000, **24**, 139-155.
48. E. Kusvuran, A. Samil, O. M. Atanur and O. Erbatur, *Appl. Catal. B* 2005, **58**, 211-216.
49. M. Pera-Titus, V. García-Molina, M. A. Baños, J. Giménez and S. Esplugas, *Appl. Catal. B* 2004, **47**, 219-256.
50. A. Fujishima, X. Zhang and D. A. Tryk, *Surf. Sci. Rep.*, 2008, **63**, 515-582.
51. F. E. Osterloh, *Chem. Soc. Rev.*, 2013, 42, 2294-2320.